Hysteretic Behavior of a Belt Tensioner: Modeling and Experimental Investigation

G. MICHON
Valeo Electrical Systems, 2 rue A. Boulle 94000 Créteil, France

L. MANIN
R. DUFOUR
Laboratoire de Dynamique des Machines et des Structures, UMR CNRS 5006, INSA de Lyon, 18 rue des Sciences 69621 Villeurbanne, France (regis.dufour@insa-lyon.fr)

Abstract: In this paper we describe the modeling of the hysteretic behavior of belt tensioners. An initial experimental device is composed only of the tensioner by using forcing frequencies, preloads and deflection amplitudes. It permits the identification of the parameters of the restoring force model used. Comparison of the measured and predicted force–deflection loops of the tensioner subjected to large deflections permits preliminary validation of the model. The second experimental device consists of a belt-tensioner system. Its non-linear modeling includes the above hysteretic model and the belt's longitudinal characteristics. Validation of the belt-tensioner model is completed by comparing the measured and predicted belt tension. Finally, it is shown by using a parametric investigation and phase-plane portrait that the response of the belt-tensioner system increases with the frequency and the amplitude of the excitation.

Key Words: Damper, belt, tensioner, hysteresis

1. INTRODUCTION

Mechanical tensioners are widely used in belt drive systems. They play a predominant role in the dynamic behavior of the belt: they maintain nominal tension in the slack span and reduce the transverse vibration level, especially in the automotive serpentine belt drive system (Beikmann et al., 1997). This type of mechanical system, known as a front-end accessory drive (FEAD), gives rise to many current technological challenges and scientific problems (see, for example, Kwon and Ih, 2000; Leamy and Wasfy, 2002; Cheng and Zu, 2003; Parker, 2004). Satisfying such industrial requirements calls for a device with a complicated design. Roughly speaking, this consists of a rotating device composed of different mechanical parts (spring, end-stops) and different types of contact (dry and lubricated). This type of design leads to considerable non-linear behavior due to stick–slip motion (Leamy and Perkins, 1998) and difficult identification of parameters, such as stiffness, dry friction, and viscous damping. Consequently, the establishment of a complete model based on the combination of classical models, as formulated by Maxwell, Kelvin–Voigt, and Prandtl, is not obvious

DOI: 10.1177/1077546305055539

(see, for example, Kraver et al., 1996). It therefore appears logical to use the restoring force model proposed by Al Majid and Dufour (2002, 2004), which depends, in particular, on preload, forcing frequency, and amplitude of deflection. Its efficiency has been demonstrated with a continuous system equipped with localized non-linearity subjected to both impacts and harmonic excitation.

In order to improve the modeling accuracy of a global belt drive system containing a tensioner, in this paper we present a non-linear model of a real belt-tensioner system capable of strong dissipation essentially due to stick–slip motion. Its modeling uses an experimental and theoretical approach. Section 2 is devoted to the application of the restoring force model on the tensioner. A specific experimental setup is assembled to measure the force–deflection loops of the tested tensioner subjected to several preloads and forcing frequencies for a given deflection amplitude. Moreover, these experiments are performed in order to adjust the parameters of the tensioner model. In Section 3, the tensioner is implemented in a simple belt-tensioner system. In particular, the discrete modeling of the associated experimental device takes into account the hysteretic tensioner model and the longitudinal characteristics of a real belt. The harmonic response uses a classical time integration method. The predicted and measured results are then compared to validate the tensioner model. Phase-plane portraits are investigated.

2. TENSIONER MODEL

2.1. General Hysteretic Model

The rotational hysteretic behavior of the tensioner can be described by a first-order differential equation (see, for example, Al Majid and Dufour, 2004), which combines the restoring torque R_θ and the angular deflection θ as follows:

$$\dot{R}_\theta = \beta\dot{\theta}\left(h - R_\theta \operatorname{sgn}\dot{\theta}\right). \tag{1}$$

Here, $\dot{} = \dfrac{d}{dt}$, where t is the time, β is a positive constant, and h is closely related to the asymptotic function of R_θ versus θ. Function h can be the upper h_u or lower h_l asymptotic lines depending on the sign of the speed of angular deflection according to

$$h = \frac{1}{2}\left((h_u + h_l)\operatorname{sgn}\dot{\theta} + (h_u - h_l)\right). \tag{2}$$

If necessary, h can be also a function of the initial angular position θ_0 and of the forcing frequency Ω. The upper and lower asymptotic lines are approximated using a polynomial expansion:

$$h_u(\theta_0, \Omega) = \sum_{i=0}^{n} a_i(\theta_0, \Omega)\theta^i, \tag{3}$$

$$h_l(\theta_0, \Omega) = \sum_{i=0}^{n} b_i(\theta_0, \Omega)\theta^i. \tag{4}$$

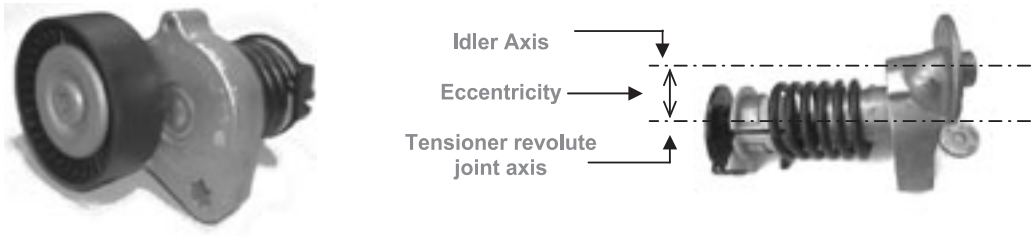

Figure 1. The tensioner tested.

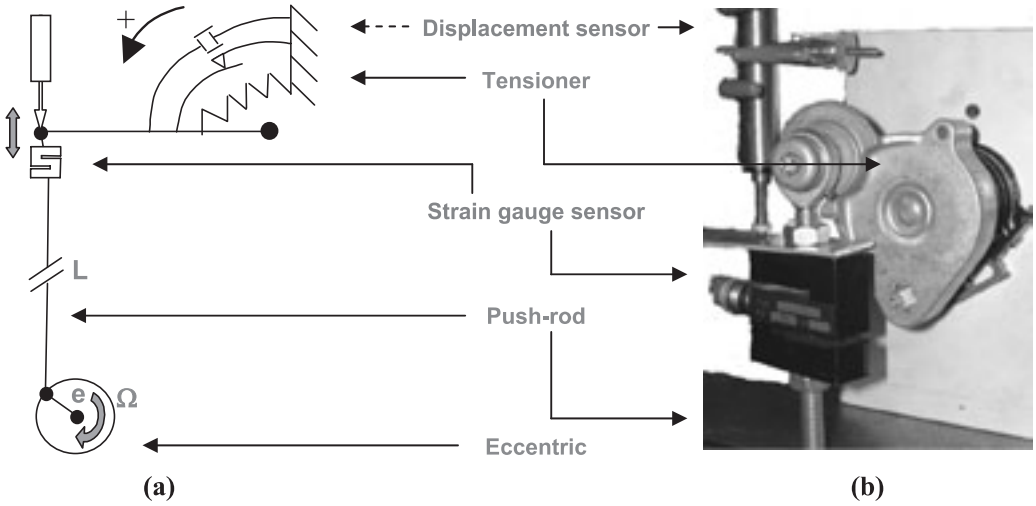

Figure 2. Schematic view (a) and photograph (b) of the test rig 1.

In what follows, coefficients a_i and b_i are identified experimentally.

2.2. Experimental Bench Test

Figure 1 shows the tested tensioner and its exploded view. It is used in an automotive front-end accessory belt drive and is composed of two collinear shafts on which the idler, torsional spring and end-stops are connected by either oiled or dry contacts.

The tensioner is implemented on an experimental test bench in order to demonstrate its behavior. Its base is fixed on a very stiff frame, while its eccentric shaft is linked to a slider-crank mechanism activated by an electrical motor. Figure 2 gives a schematic view (a) and a photograph (b) of the experiment. The length of the rigid connecting rod is long enough to assume that the excitation of the tensioner is a pure sine:

$$\theta(t) = \theta_0 + \theta_1 \sin(\Omega t). \tag{5}$$

Forcing frequency Ω, excitation amplitude θ_1 and preload θ_0 are adjusted by the speed of rotation of the electrical motor, the eccentric of the crank, and the length of the connecting rod, respectively. The ranges of these three parameters are 0–300 rpm, 3.5–10 mm, and 795–805 mm, which correspond to the values observed during an engine startup.

A strain gage sensor and an inductive displacement probe permit simultaneous measurement of the transmitted force and the displacement exerted on the tensioner by the connecting rod. A data post-processing method developed with MATLAB® filters and converts the force–displacement loop into a torque–angular displacement loop.

2.3. Identification Tests

The identification tests were carried out when the heating temperature was reached, i.e. when there was no more evolution of the measured loops.

Let test 1 be performed with a constant speed of rotation of 100 rpm. Figure 3(a) shows the general shape of the measured loop. Schematically, the motion of the tensioner is close to a stick–slip motion. Parts 1 and 3 are devoted to the stick motion, while parts 2 and 4 are devoted to the slip motion. The design of the tensioner and its assembly in the experimental setup introduce a composed bending and torsion loading: the contact pressure increases during parts 1 and 2, and decreases during parts 3 and 4. The slope of parts 1 is mainly due to the bending stiffness of the pivot axis. The transition between stick and slip motions is shifted while the normal force on the contact area increases. The slope of part 2 is due to the torsional spring stiffness and the tangential pressure on the contact.

As the loop area corresponds to the dissipation, we can conclude that a high dissipative effect is obtained.

Test 2 focuses on the role of the preload (Figure 4(a)). Three initial angular positions are investigated (6°, 14°, and 22°), while the alternative deflection amplitude remains constant (5.3°). It should be mentioned that an end-stop phenomenon slightly deforms the 6° loop. Nevertheless, it can be observed that the higher the initial deflection, the higher the dissipative effect becomes. The preload increases the normal force on the pivot axis and consequently the stick–slip threshold.

In test 3, three different speeds of rotation (9, 19, and 29 rad s^{-1}) are used while the alternative deflection amplitude remains constant (see Figure 5(a)). The higher the forcing frequency, the higher the dissipative effect becomes. A slight frequency dependence due to the lubricated contact, as mentioned in Section 2.2, is observed.

2.4. Asymptotic Line Identification

The identification tests have shown that load–deflection loops are bounded by upper and lower lines which are assumed here to be straight:

$$h_u(\theta_0, \Omega) = a_1(\theta_0, \Omega)\theta + a_0(\theta_0, \Omega), \tag{6}$$

$$h_l(\theta_0, \Omega) = b_1(\theta_0, \Omega)\theta + b_0(\theta_0, \Omega). \tag{7}$$

The effects of the initial angular deflection, i.e. preload, and the forcing frequency on the measured loops permit expanding the coefficients a_0, a_1, b_0, b_1 as follows

$$a_1 = -0.0057\Omega + 0.3376, \quad b_1 = a_1/2, \tag{8}$$

$$a_0 = 0.0014(\theta_0 + 129)(\Omega + 162), \quad b_0 = 12, \tag{9}$$

with Ω in rad s^{-1} and θ_0 in degrees.

Obtaining β can be made by equaling theoretical and experimental dissipated energy, i.e. the area defined by the loop. The linear expansions (6) and (7) make possible the analytical integration of equation (1). In the case of a positive deflection velocity, equation (1) becomes

$$\frac{\mathrm{d}R_{\theta u}}{\mathrm{d}t} = \beta\dot{\theta}\left(h_u - R_{\theta u}\right), \tag{10}$$

where $R_{\theta u}$ is the upper restoring torque. The integration gives

$$R_{\theta u}(\theta) = K_u \mathrm{e}^{-\beta(\theta-(\theta_0-\theta_1))} + a_0 + a_1\theta - \frac{a_1}{\beta}. \tag{11}$$

The integration constant K_u is expressed by using the value of $R_{\theta u}$ at $\theta = \theta_0 - \theta_1$:

$$K_u = \frac{a_1}{\beta} - a_0 - a_1(\theta_0 - \theta_1) + R_{\theta u}|_{\theta=\theta_0-\theta_1}. \tag{12}$$

In the case of a negative deflection velocity, equation (1) is

$$\frac{\mathrm{d}R_{\theta l}}{\mathrm{d}t} = \beta\dot{\theta}\left(-h_l + R_{\theta l}\right), \tag{13}$$

where $R_{\theta l}$ is the lower restoring torque. The integration gives

$$R_{\theta l}(\theta) = K_l \mathrm{e}^{\beta(\theta-(\theta_0+\theta_1))} + b_0 + b_1\theta + \frac{b_1}{\beta}. \tag{14}$$

The integration constant K_l is expressed by using the value of $R_{\theta l}$ at $\theta = \theta_0 + \theta_1$:

$$K_l = -\frac{b_1}{\beta} - b_0 - b_1(\theta_0 + \theta_1) + R_{\theta l}|_{\theta=\theta_0+\theta_1}. \tag{15}$$

The dissipated energy E_{mod} provided by the model corresponds to the difference of the works of upper and lower restoring torques

$$E_{mod} = \int_{\theta_0-\theta_1}^{\theta_0+\theta_1} (R_{\theta u} - R_{\theta l})\,\mathrm{d}\theta, \tag{16}$$

$$E_{mod} = \frac{1}{\beta}\left(\mathrm{e}^{-2\beta\theta_1}(K_l - K_u) + (K_u - K_l) + 2\beta\theta_0\theta_1(a_1 - b_1) + 2\beta\theta_1(a_0 - b_0)\right.$$
$$\left. - 2\theta_1(a_1 + b_1)\right), \tag{17}$$

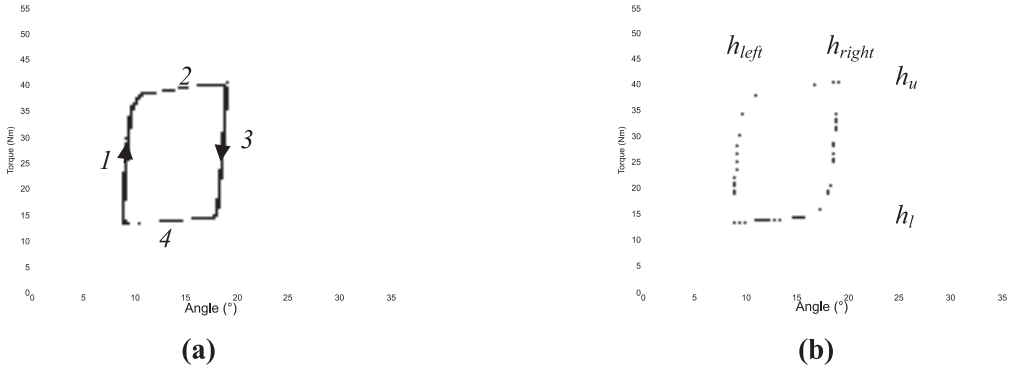

Figure 3. Measured (a) and simulated (b) torque–angular deflection loops obtained at 100 rpm.

Figure 4. Influence of initial angular position (6°, 14°, and 22°) on the torque–angular deflection loops.

in which all constants, except β, are known. Actually, the experimental energy E_{exp} dissipated by the tensioner is obtained by evaluating the approximated area of the loops defined by the four straight lines, h_u, h_l, h_{left}, and h_{right} (see Figure 3). The equality $E_{mod} = E_{\text{exp}}$ yields the value $\beta = 2.0$.

Consequently, the three tests described previously can be numerically simulated and the associated numerical loops obtained with MATLAB® and plotted in Figures 3(b), 4(b), and 5(b) are quite close to the experimental ones.

In order to ensure the model is reliable, the device is subjected to a large deflection in test 4; see the measured loop plotted in Figure 6(a). The associated simulation permits obtaining the numerical loops plotted in Figure 6(b). The comparison of the predicted and measured loops is satisfactory in spite of the end-stop phenomenon observed close to 0° angular deflection.

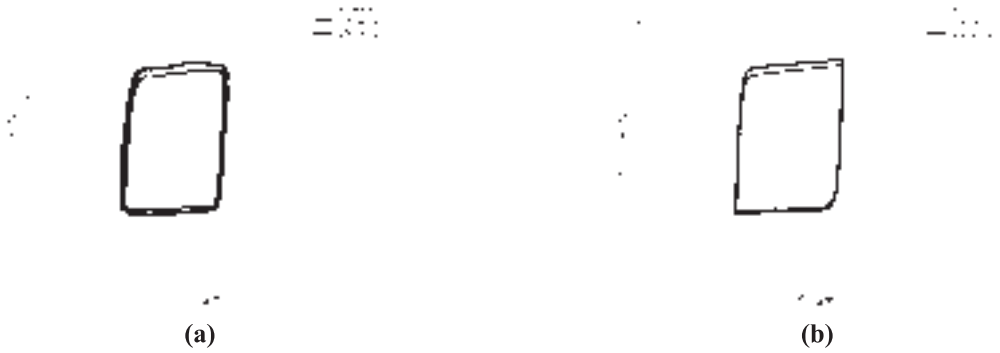

Figure 5. Influence of forcing frequency (9, 19 and 29 rad s^{-1}) on the torque–angular deflection loops.

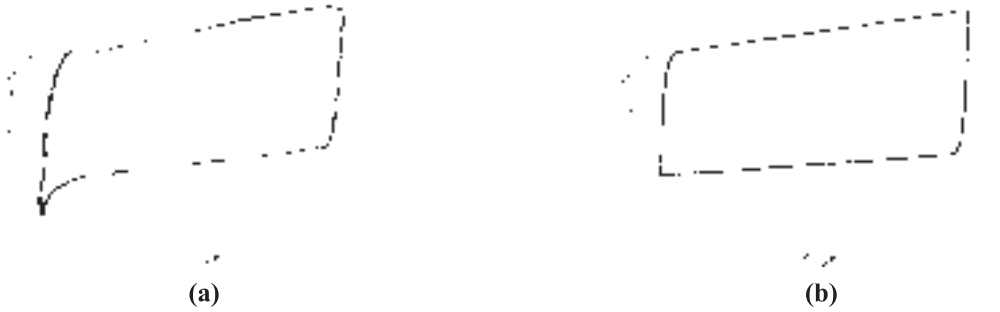

Figure 6. Restoring torque of the tensioner subjected to large angular deflection amplitude.

3. EXPERIMENTAL VALIDATION ON A SIMPLE BELT-TENSIONER SYSTEM

The previous section was devoted to the parameter identification of the tensioner model expressed using restoring torque and angular deflection. The current section concerns the implementation in a multi-degrees-of-freedom (MDOF) mechanical system of the tensioner model expressed using restoring force and deflection. This is carried out by using an academic device investigated experimentally and numerically.

3.1. The Simple Belt-tensioner System Tested

The investigated device is composed of the tensioner equipped with a pulley wrapped in an industrial multi-ribbed belt. The belt is linked to an S-shaped load cell subjected to an alternative displacement exerted by the rotation of an eccentric (see Figure 7). This type of device uses only the longitudinal characteristics of the belt.

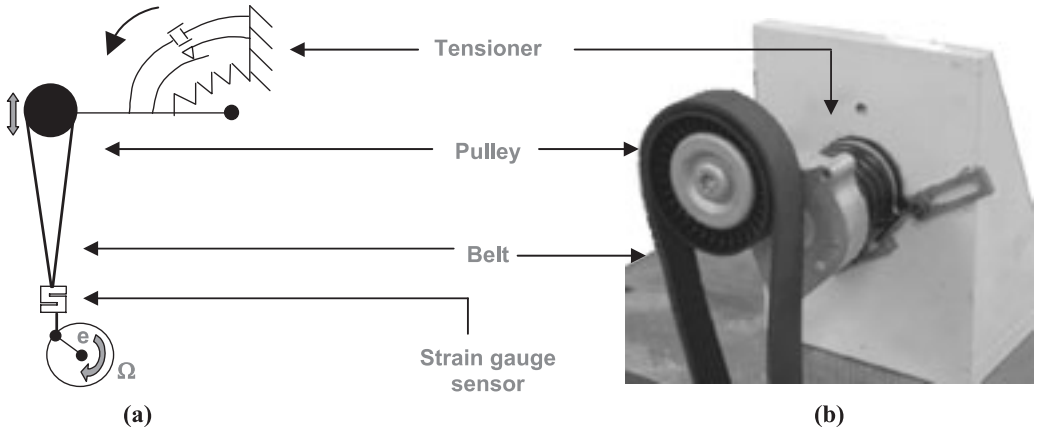

Figure 7. Schematic view (a) and photograph (b) of the test rig 2 devoted to the validation test.

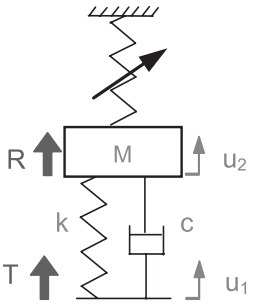

M = 0.150 kg
k = 560 kN m^{-1}
c = 6.4 N s m^{-1}

U_0 = 5 mm
U_1 = 3 mm
Ω = 8.8 rad s^{-1}

(b)

Figure 8. Belt-tensioner model.

3.2. Response to a Sine Excitation

Figure 8 shows the model of the belt-tensioner device. The belt is modeled with two DOF, u_1 and u_2. The longitudinal stiffness k and damping c of the belt were obtained by using an experimental modal analysis, not presented here. Here, the influence of tensioner rotation is expressed by longitudinal motion u_2. Let M be the mass of the pulley, T the tension of the belt, and R the restoring force given by the tensioner taking into account the hysteretic behavior of the tensioner.

Consequently, the dynamic behavior of the academic device described is governed by the two following classical differential equations

$$c\left(\dot{u}_1 - \dot{u}_2\right) + k\left(u_1 - u_2\right) = T\left(t\right) \tag{18}$$

$$M\ddot{u}_2 + c\dot{u}_2 + ku_2 = R\left(u_2\right) + c\dot{u}_1 + ku_1 \tag{19}$$

Figure 9. Transient phase-plane portrait at DOF 2.

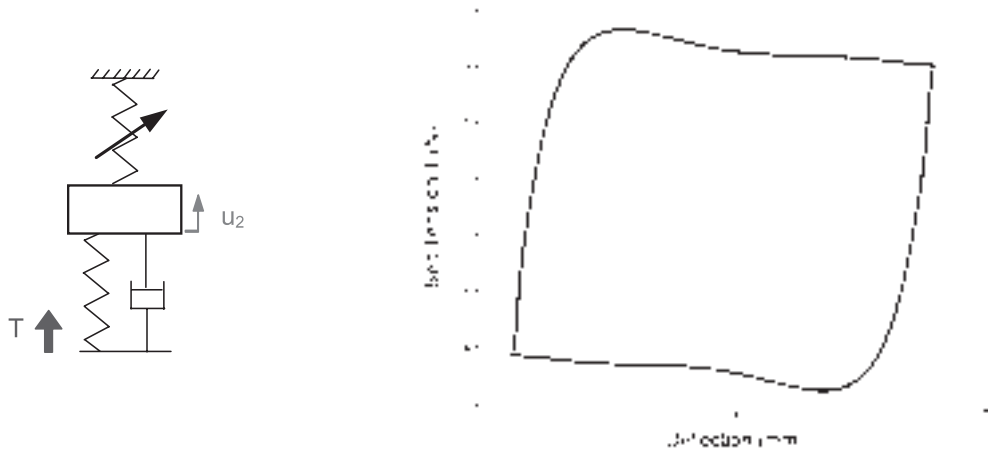

Figure 10. Predicted belt tension–deflection loop.

coupled with the first-order differential equation describing the hysteretic behavior of the tensioner

$$\dot{R} = \beta \dot{u}_2 \left(h - R \operatorname{sgn}\left(\dot{u}_2\right)\right). \tag{20}$$

The following imposed displacement

$$u_1(t) = U_0 + U_1 \sin(\Omega t), \tag{21}$$

forces the deflection of the 2-DOF system. The response to this sine excitation is obtained by using SIMULINK–MATLAB® software and the classical RK-4 time integration method. The initial conditions at $t = 0$ are $u_2(0) = \dot{u}_2(0) = R(0) = 0$ and the time-step is 10^{-5} s.

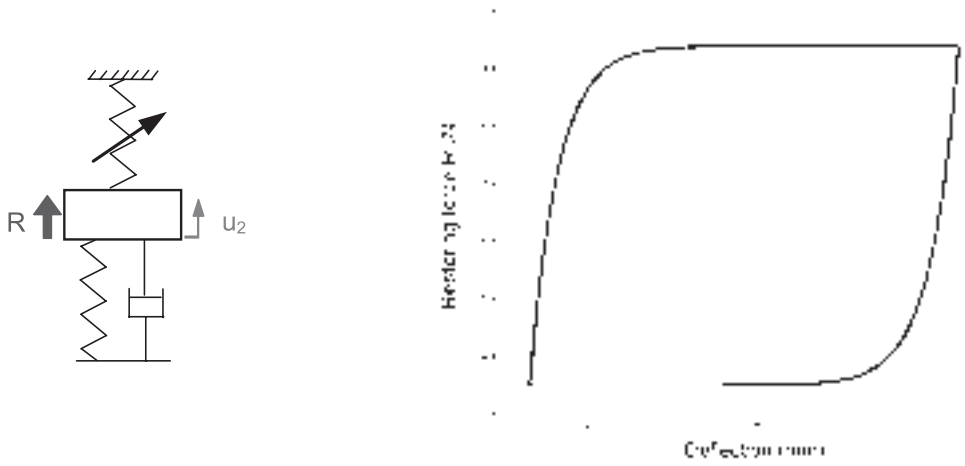

Figure 11. Predicted restoring force–deflection loop.

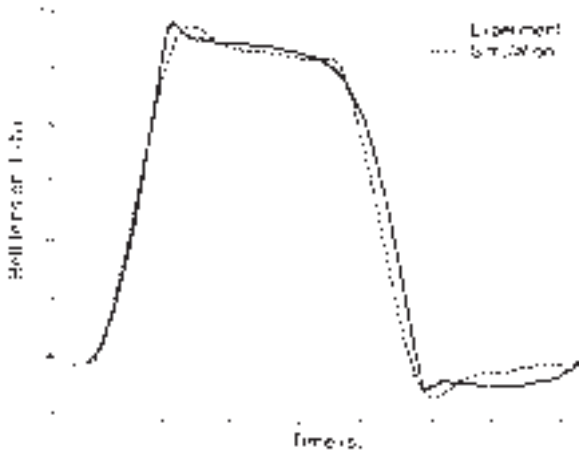

Figure 12. Time history predicted and measured belt tension.

The steady-state behavior is rapidly achieved due to the presence of high dissipation. See the phase-plane portrait predicted at DOF 2 and plotted in Figure 9.

Figures 10 and 11 show the predicted belt tension–deflection loop and restoring force–deflection loop, respectively, obtained during steady-state behavior. The comparison of these two loops shows a difference due to the transfer function of the belt. In the case of rigid link (i.e. the belt has an infinite stiffness) the loop in Figure 10 fits the loop in Figure 11.

The time histories of the predicted and measured belt tension are compared in Figure 12. On the basis of this experimental validation, it is demonstrated that the proposed model is satisfactory.

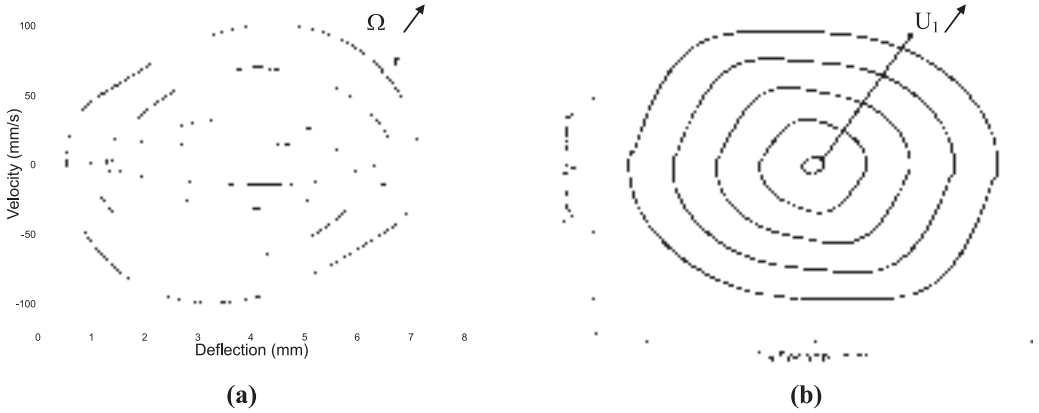

Figure 13. Steady-state phase-plane portrait of DOF 2 versus forcing frequency (a) and deflection amplitude (b).

3.3. Parametric Response

After validation, the model was subjected to several forcing frequencies and deflection amplitudes within the usual operating range. Taking into account the assumptions made on the belt and the tensioner model, the predicted phase-plane portraits of the DOF 2 versus four forcing frequencies (5, 10, 20, and 30 rad s^{-1}) versus five deflection amplitudes (1, 3, 5, 7, and 9 mm) are plotted in Figure 13(a) and (b) respectively. Each limit loop is obtained with 10 cycles. The limit loops are stable and increase monotonically versus the forcing frequency or versus deflection amplitude because no resonance phenomenon is reached in the forcing frequency range. Moreover, it can be observed that the rugged shape vanishes with the forcing frequency (see Figure 13(a)): the elasticity of the belt and the inertia of the device filter the stick–slip phenomenon exhibited by loops 5, 10, and 20 rad s^{-1}.

4. CONCLUSION

A hysteretic model was used to model the behavior of a belt tensioner mainly functioning with stick–slip motion. The parameters of the tensioner model were identified by three experimental tests with preload, forcing frequency, and deflection amplitude. The proposed tensioner model can be implemented in the global model of the automotive front-end accessory drive especially during engine startup.

The experimental belt-tensioner device permitted validating the tensioner model implemented in 2 DOF, i.e. the belt. Finally, by using a parametric investigation and phase-plane portrait, it is shown that the response of the belt-tensioner system increases with the frequency and the amplitude of the excitation for possible operating ranges.

REFERENCES

Al Majid, A. and Dufour, R., 2002, "Formulation of a hysteretic restoring force model. Application to vibration isolation," *Nonlinear Dynamics* **27**, 69–85.

Al Majid, A. and Dufour, R., 2004, "Harmonic response of a structure mounted on an isolator modeled with a hysteretic operator: experiment and prediction," *Journal of Sound and Vibration* **277**, 391–403.

Beikmann, R. S., Perkins, N. C., and Ulsoy, A. G., 1997, "Design and analysis of automotive belt drive systems for steady-state performance," *ASME Journal of Mechanical Design* **119**, 162–168.

Cheng, G. and Zu, J. W., 2003, "Non-stick and stick–slip motion of a Coulomb-damped belt drive system subjected to multifrequency excitations," *ASME Journal of Applied Mechanics* **70**, 871–884.

Leamy, M. J. and Perkins, N. C., 1998, "Nonlinear periodic response of engine accessory drives with dry friction tensioners," *ASME Journal of Vibration and Acoustics* **120**, 909–916.

Leamy, M. J. and Wasfy, T. M., 2002, "Transient and steady-state dynamic finite element modeling of belt drives," *ASME Journal of Dynamics Systems, Measurement, and Control* **124**, 575–581.

Kraver, T. C., Fan, G. W., and Shah, J. J., 1996, "Complex modal analysis of a flat belt pulley system with belt damping and Coulomb-damped tensioner," *ASME Journal of Mechanical Design* **118**, 306–311.

Kwon, Y. I. and Ih, J-G., 2000, "Vibrational power flow in the moving belt passing through a tensioner," *Journal of Sound and Vibration* **229**, 329–353.

Parker, R. G., 2004, "Efficient eigensolution, dynamic response, and eigensensitivity of serpentine belt drives," *Journal of Sound and Vibration* **270**, 15–38.